Fuel 431 (2027) 141936



Contents lists available at ScienceDirect

Fuel

journal homepage: www.elsevier.com/locate/jfue



Full Length Article

Influence of Si on the combustion process of micron-sized iron particles

Z. Bruyr[a,*], L. Ahmad[a], L. Choisez[a], M. Gilles[a], L. Jeanmart[a], F. Halter[b], F. Contino[a]

[a] Institute of Mechanics, Materials and Civil Engineering (iMMC), Université catholique de Louvain (UCLouvain), Place du Levant, 2, 1348, Louvain-la-Neuve, Belgium
[b] CNRS – ICARE, University Orléans, Avenue de la Recherche Scientifique, 45071 Cedex 2, Orléans, France

HIGHLIGHTS

- Fe-7Si particles feature more difficult ignition due to the creation of a Si-rich oxide layer.
- Ignited particles oxidize in the liquid state until they reach magnetite.
- Combustion products consist of dendritic structures with a eutectic phase in the interdendritic region.
- Particles exhibit a multi-peak luminosity profile due to the formation of a Si-rich oxide layer that limits internal diffusion.
- Overall, Si increases the combustion time and modifies the combustion regime toward internal-diffusion-limited behavior.

ARTICLE INFO

Keywords:
Renewable metal fuels
Energy storage
Iron
Single-particle
Silicon
Impurities

ABSTRACT

The use of impure powders in the metal-fuel cycle could reduce powder production costs, enable the valorization of underutilized feedstocks, and limit competition with the steel industry. However, the influence of impurities on the combustion process remains poorly understood. Silicon is one of the potential impurities present in low-cost iron sources, and the objective of this work is to investigate its impact on the combustion behavior of micron-sized iron particles. To this end, an Fe-7Si powder was studied using both single-particle and multi-particle combustion setups, enabling *in situ* visualization and *ex situ* microstructural analysis, respectively. In the multi-particle burner, the Fe-7Si powder featured limited conversion efficiency (0.1%–6.2%) in the reference preheating conditions. This efficiency increased at higher preheating temperature (26.3%–39% at 930 °C). This suggests that Si significantly affects particle ignition, likely through the formation of a Si-rich oxide layer. Nevertheless, once ignited, particles undergo nearly complete oxidation in the liquid state, reaching magnetite as the main oxide phase. The resulting combustion products consist of dendritic structures. A eutectic phase is also detected in the interdendritic region, with a Si enrichment compared to the dendrites. Its presence arises during solidification after reaching the eutectic point associated with a complete oxidation in the liquid state. In the single-particle burner, particles exhibit a multi-peak luminosity profile characterized by an initial small peak, likely associated with the formation of a silicon-rich oxide layer that limits internal diffusion. This stage is followed by a second luminosity increase during which new oxide spots appear at the particle surface, suggesting the formation of iron oxide penetrating the previously formed oxide layer. Overall, Si increases the combustion time of iron particles and modifies the combustion regime toward an internal-diffusion-limited behavior. However, Fe-7Si particles are still able to burn successfully in the liquid state, provided that ignition is achieved.

1. Introduction

The current transition from fossil fuels to renewable energy sources requires energy storage and transport [1], on both a daily and seasonal basis. Seasonal storage could be achieved using metal fuels [2]. Among them, iron is a particularly attractive candidate because it is abundant, low cost, can be transported safely over long distances, and can be stored safely on a long-term basis. Micron-sized iron particles burn in air to release the stored energy, while the combustion products retain a similar size to the introduced particles. They can subsequently be collected and reduced back to their initial state using green hydrogen, closing the so-called Metal-enabled Cycle of Renewable Energy (MeCRE).

To help design effective commercial burners, the study of iron particle combustion has received considerable research interest. Notably, single-particle experimental [3–8] and numerical studies [9–13] have significantly improved our understanding of the liquid-state combustion

* Corresponding author.
Email address: zakarie.bruyr@uclouvain.be (Z. Bruyr).

https://doi.org/10.1016/j.fuel.2026.141936
Received 8 June 2026; Received in revised form 30 September 2026; Accepted 25 October 2026
Available online 2 November 2026
0016-2361/© 2026 Elsevier Ltd. All rights are reserved, including those for text and data mining, AI training, and similar technologies.

process. Nevertheless, these studies used high-purity iron powder (>99 wt.% Fe), whereas using low-grade iron ores or other low-cost iron feedstocks could reduce powder production costs, allow the valorization of unused sources, and avoid competing with steel industry. However, those iron sources may contain a significant amount of varying impurities [14]. Therefore, it is crucial to better understand the influence of these impurities on the combustion process.

Even though it remains limited, interest in the use of impure iron powders is growing. The impact of the presence of up to 20 wt.% of four metal oxide impurities (Al_2O_3, SiO_2, MnO, CaO) was numerically investigated [15], suggesting that they decrease the peak temperature without impacting the total heat release, but also potentially create a complex ternary oxide phase by reacting with iron oxide which may prevent complete oxidation and reduction. The presence of 1.5 wt.% impurities of Mn, Al, and Si oxides in recycled mill scale powder reduced its ignition efficiency (89–96% for the mill-scale *vs.* 95–97% for pure Fe) [16], but still allowed a stable flame to form [17]. Moreover, a multiple and complex evaporation process took place, with the formation of mixed Cu, Ni, Mn, Fe oxide nanoparticles containing traces of Mg and Ca, and individual Si and Cr oxide nanoparticles [16]. Direct reduced iron (DRI) particles containing up to 5.2 wt.% oxide impurities (mainly SiO_2, Al_2O_3, and MnO) were also successfully burned in an open-flame propane burner [18]. These combusted particles showed a different pore distribution than pure Fe due to the presence of silicon oxide which increases the oxygen solubility of the liquid oxide, subsequently limiting the oxygen gas release during solidification. Concerning metallic impurities, the influence of 5 wt.%, 9 wt.%, and 20 wt.% Al on iron combustion process was experimentally studied in both a single-particle and multi-particle burner [19]. This work showed that the particles burn in an intermediate regime between the heterogeneous surface combustion of Fe and the gas-phase combustion of Al. Overall, the presence of impurities impacts the oxidation rate, the combustion time, and the evaporation dynamics.

Another metallic impurity present in recycled steel is Si, with up to 6 wt.% in electrical steels [20,21]. The first single-particle experimental study of the combustion of Si-containing particles was performed by Peng et al. [22]. They showed that the combustion of Fe-6.2Si particles follows a multi-peak luminosity evolution. They suggest that after ignition, the particle burns in an external-diffusion-limited regime until the formation of a silicon oxide layer mitigates oxidation, creating the first small peak. The luminosity then decreases suggesting that internal diffusion is limiting the oxidation rate. Then, a luminosity jump occurs and the luminosity rises again. A second small peak similar to the first one may take place, leading to the same pattern. Finally, the luminosity rises to a higher level to eventually reach a larger peak, preceded by a luminosity jump and followed by the cooling and solidification spearpoint. The luminosity jump prior to the large peak is suggested to be associated with a sudden inflation event potentially provoked by the presence of hydrogen [23].

In this study, the influence of Si on the combustion process of micron-sized iron particles is investigated using a multi-scale approach. On one side, Fe-7Si particles are laser-ignited in a single-particle electrodynamic levitator coupled with a color camera enabling high-resolution and high-speed *in situ* imaging and a luminosity acquisition system. This allows us to extend the experimental conditions in which Fe-Si particles are burned (highly preheated particles burning in ambient conditions), and to compare the measured luminosity evolution with the results of Peng et al. [22]. Moreover, the recorded videos of the combustion provide insightful interpretation about the liquid phases configuration occurring at the particle surface. On the other side, the same Fe-7Si particles are burned in a 5 kW multi-particle tornado burner, allowing us to estimate the influence of Si on the ignition efficiency and to collect combustion products or unignited particles to investigate their microstructure. Together, the multi-scale approach enables the combination of *in situ* and *ex situ* measurements to fully understand the whole combustion process of Fe-Si particles.

Table 1
Initial powder composition in weight percent measured by ICP and sulfur combustion.

[wt.%]	Fe	Si	Cu	C	Cr	Ni	Mn	Co	S	O
Fe-7Si	92.7	7	0.01	0.01	0.08	0.02	0.08	0.01	<0.02	Bal.

2. Methods

2.1. Powders

The Fe-7Si particles used in this study were produced by gas atomization from cast alloys by Sandvik. They were sieved between 25 μm and 63 μm before being burned in each setup. The powder composition measured using Inductively Coupled Plasma (ICP) and carbon and sulfur combustion measurements is listed in Table 1. The uncertainty in the composition is ±3% (relative to the measured value) for elements present in quantities greater than 1 wt.% and ±0.01 wt.% for other elements. Moreover, measurements using an Energy Dispersive X-ray Spectrometer (EDS) on particle cross-sections show small chemical variations between individual particles (6.89 ± 0.47 wt.% of Si and 93.11 ± 0.47 wt.% of Fe, measured on 40 particles) and within a single particle (6.71 ± 0.13 wt.% Si and 93.29 ± 0.13 wt.% Fe, measured on 6 points inside a single particle). The thickness and composition of the native oxide layer were also characterized using X-ray Photoelectron Spectroscopy (XPS). The results indicate a native oxide layer with a thickness higher than the XPS probing depth of 10 nm (see Supplementary Materials SM1).

2.2. Single-particle levitator

The Fe-7Si particles were burned inside a single-particle electrodynamic levitator allowing for *in situ* high-speed imaging and luminosity measurement during the combustion process. Initially, each particle was suspended within the combustion chamber by electrostatic forces generated using AC and DC electrodes (see Fig. 1), and subsequently ignited using a CO_2 laser. Upon ignition, the particle followed a downward trajectory while combusting in ambient air. The combustion process was captured by a high-speed color camera (PHANTOM T-2410) operating at 25 kHz, coupled with a QUESTAR QM 100 teleobjective, providing a magnification of 1.5 μm/pixel (see Fig. 2). The field of view of the camera is a square of 767 × 767 pixels. Additionally, the temporal evolution of the particle's luminosity was measured using THORLABS PMT1002 photomultiplier tubes (PMTs). A detailed description of the experimental setup is beyond the scope of this paper; readers are referred to prior publications for comprehensive information [8,24,25].

The snapshots recorded by the camera allow us to (1) measure the size evolution of the particles during the combustion and (2) observe surface phenomena between distinguishable phases, depending on their surface emissivity. The methodology for size measurement is detailed in Supplementary Materials SM2 and is associated with an uncertainty of ± 1.5 μm. Concerning surface emissivity, typical values for liquid iron and liquid iron oxide between 2030 K and 2700 K are 0.35 and 0.7, respectively [26]. As observed in our previous study [8], this gap is high enough to distinguish the two phases. The emissivity of silicon is around 0.2 [27,28], while measurements for liquid silicon oxide are scarce. It is only known that the liquid-state emissivity of silica lies between 0.6 and 0.8 and increases with temperature [29,30]. Therefore, the distinction between metallic and oxide phases is also possible for Si and its oxide, but regarding the uncertainty and the close values for iron and silicon oxide phases, it is difficult to predict which will be brighter between the two.

2.3. Multi-particle tornado burner

The same powder was also burned inside a 5 kW multi-particle burner. It allows to collect the combustion products and measure their

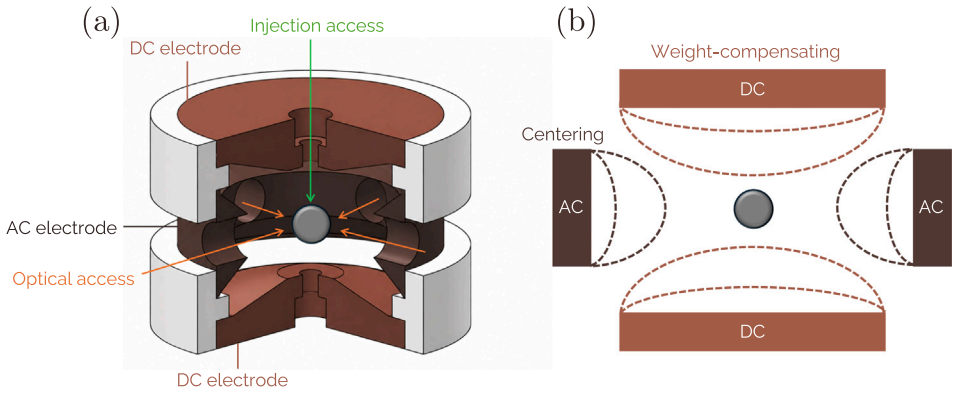


Fig. 1. Schematic of (a) the electrodynamic levitator (including the injection access and the 4 optical accesses) and (b) the electric lines created by the DC and AC electrodes to compensate for the particle weight and center it, respectively. For clarity, the particle is depicted as larger than its actual size.

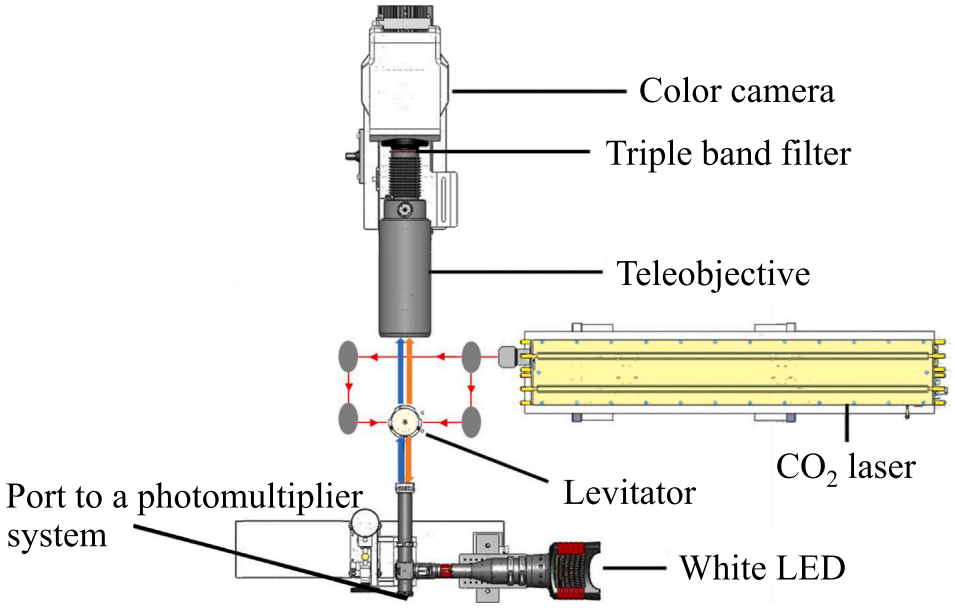


Fig. 2. Schematic of the full experimental setup including the pathways of the CO_2 laser beam (red arrows), the LED light (blue arrows) and the radiative emissions from the combustion (Orange arrows). (For interpretation of the references to colour in this Figure legend, the reader is referred to the web version of this article.)

oxidation state and microstructure. This burner also allows to estimate the impact of the presence of 7 wt.% Si on powder ignition. This often called *tornado burner* or *MC2 burner* has already been used for several studies proving its ability to burn pure iron particles [31–33]. A succinct description of this burner follows, but the interested reader can find more details in the mentioned publications.

The burner consists of a gas flow control system, a powder dispersion system, a combustion chamber, and a cyclone collector (see Fig. 3). First, the gas flow control system is used to manage the incoming gas flows injected into the combustion chamber, ambient air in this case. Second, the dispersion system consists of a bottle that stores the powder which is agitated by a vibrator to release powder into a carrier gas flow. Then, the combustion chamber is a cylinder (50 cm long with a diameter of 13 cm) made of a Pyrex tube with a stainless steel tube inside. It is surrounded by electric heaters and insulation to preheat the gas mixture before the test to a sufficient temperature to ensure powder ignition. To create a cyclonic flame, ensuring good particle circulation and increasing their residence time, the main flow containing the powder is injected at the top center, while two swirling flows of air are injected tangentially. Finally, the combusted powder and flue gases are drawn into a cyclone collector located at the bottom of the combustion chamber which separates the particles from the hot gas stream. A gas analyzer and a nanoparticle filter are also placed in the exhaust tube prior to the cyclone collector.

Visualization of the flame below the injection port is possible as a piece of insulation has been removed to create visual access. It is used by both a camera and a spectrometer which provide an estimate of the flame temperature. Three thermocouples are also used, located at the top, center and exhaust of the combustion chamber, respectively. The top thermocouple controls the radiant heaters by turning them off when the threshold preheating temperature is reached.

As the presence of Si may influence the ignition temperature, two tests each with around 100 g of powder sieved between 25 µm and 63 µm were conducted. The first was done with a preheating temperature of 810 °C, corresponding to the predicted ignition temperature of pure iron particles [34] which is similar to what has been used before in this setup [32,33]. For the second test, the preheating temperature was increased to 930 °C, the highest temperature achievable by the setup. They will be denoted LT (810 °C) and HT (930 °C), respectively. For both tests, the main and swirl flow rates are 20.5 L_N/min and 25.5 L_N/min, respectively, leading to a swirl number of 11. The powder injection rates are 0.71 g/s and 0.68 g/s, respectively. These flow rates lead to an

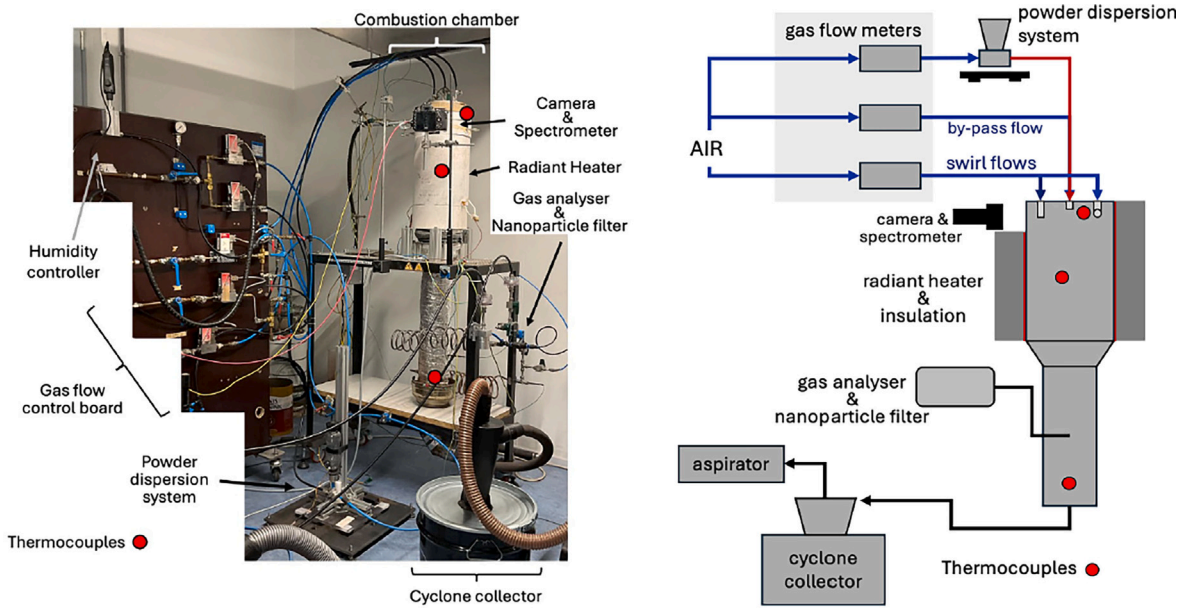


Fig. 3. Picture and schematic of the MC2 burner and its associated flows and components.

Table 2
Experimental conditions used in the MC2 burner for both Fe-7Si particles (Test LT and HT) and pure Fe particles [32,33].

Parameters	Test LT	Test HT	[32]	[33]
$T_{preheat}$ [°C]	810	930	800	810
$\dot{V}_{swirl}$ [L_N/min]	25.5	25.5	25.4	59.5
$\dot{V}_{main}$ [L_N/min]	20.5	20.5	20.5	14.7
$\dot{m}_{powder}$ [g/s]	0.71	0.68	0.5–0.8	0.6

excess air coefficient of 0.8 (based on oxidation from Fe to Fe_3O_4), corresponding to rich conditions. The experimental conditions of the two tests are summarized in Table 2 along with those used for previous pure Fe experiments in the same burner [32,33].

The combusted particles were collected both from the cyclone collector and from the walls of the combustion chamber, denoted for each test with the subscripts 'cycl' and 'wall', respectively. The collected samples were embedded and polished to be analyzed by Scanning Electron Microscopy (SEM) coupled with EDS to measure the internal phase composition of individual particles and visualize them. X-ray Diffraction (XRD) was used to identify the phases formed in the combusted powders, using a D8 Advance from Bruker with LynxEye detector, equipped with a cobalt target operating at 30 kV and 30 mA. The powders were previously crushed for the X-rays to penetrate to the center of the combusted powders. Rietveld refinement was conducted using Bruker TOPAS v5.0 software to quantify the phase distribution in the combusted powders.

3. Results

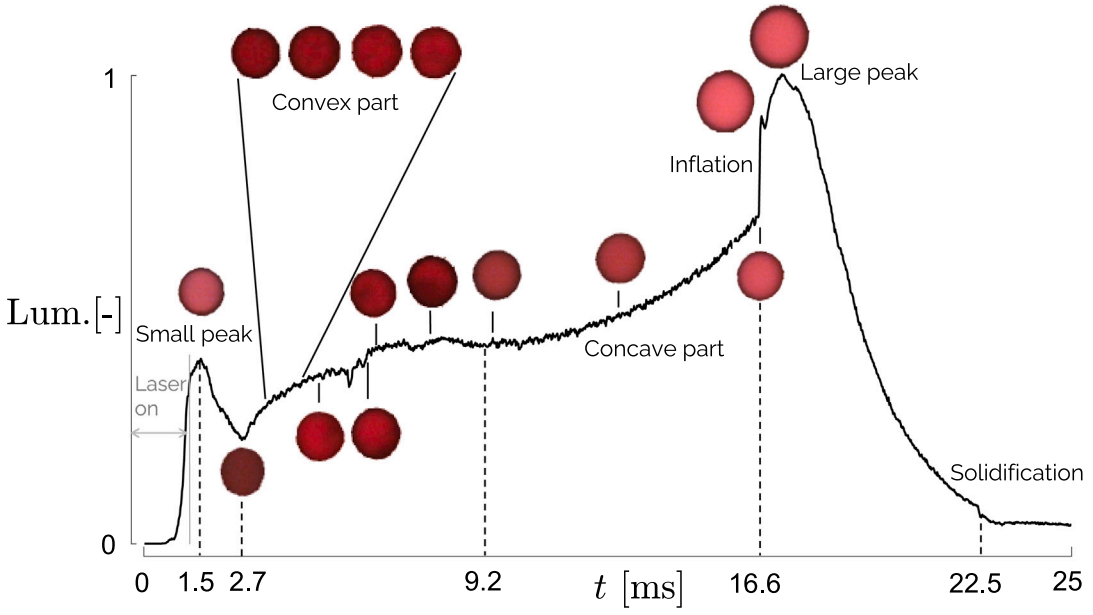
3.1. Single-particle combustion results

A total of 16 Fe-7Si particles were successfully burned in the single-particle burner, with an initial size varying between 28 and 44 microns. Similar to the previous study by Peng et al. [22], a multi-peak luminosity evolution is observed for the combustion of Fe-7Si particles (see Fig. 4). However, all the tested particles here follow the same mode of combustion with one small peak followed by a larger peak. Combustion snapshots are included in Fig. 4(a), while the influence of temperature on luminosity can be qualitatively analyzed by normalizing the luminosity signal with the size evolution (see Fig. 4b). A quantitative analysis would not be possible here because luminosity is also influenced by surface emissivity, which changes as presented below and as seen in Fig. 4(a). As in our previous study [8], the impact of changes in the distance between the particle and the luminosity acquisition system is considered negligible. This is justified by the fact that the particles leave the camera's field of view at its bottom, limiting the horizontal displacement to below half of its width (~0.5 mm), which is negligible compared to the distance of 12 cm between the center of the combustion chamber and the PM tubes.

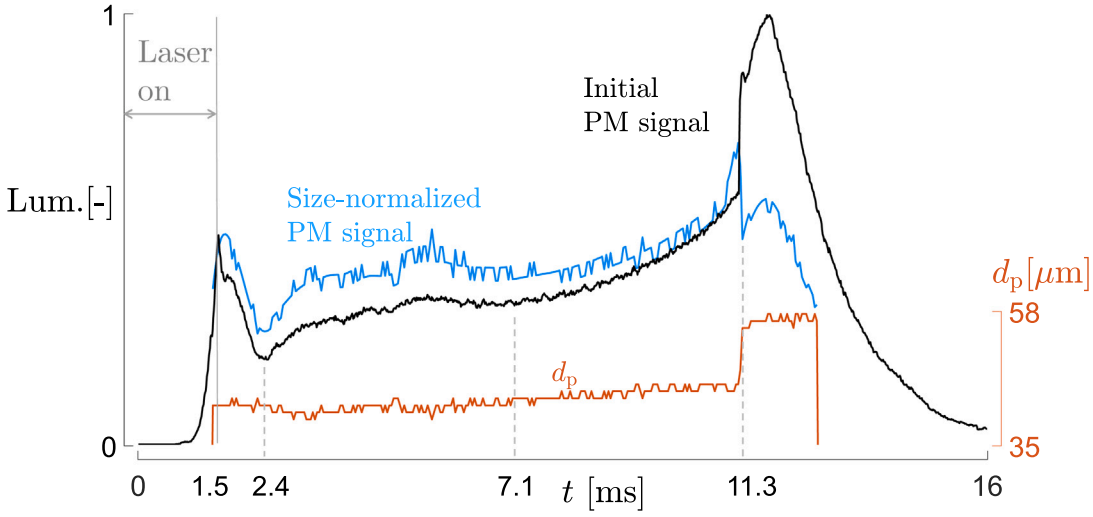
After laser heating, during which ignition and melting occur, the particles reach a first peak, called 'small peak'. It is followed by a decrease in luminosity from 0.7 ms to 1.1 ms, paired with the darkening of the particle surface (see Fig. 4a). During this luminosity decrease, the particle size slightly decreases (from 38.2 μm at the peak to 36.8 μm at the bottom), although this decrease falls within the size uncertainty range (1.5 μm). Therefore, no conclusion about the size evolution can be drawn. However, as the particle surface remains homogeneous, but only darkens, the decrease in luminosity is suggested to result from a temperature decrease.

Then, the luminosity increases again, with two successive sections with convex and concave shapes, respectively. During the convex section, a different phase from the one already present progressively appears at the surface, replacing the former phase. At first, small circular spots of the new phase arise over the entire surface (see Fig. 4a). Then, they progressively grow in size and coalesce, until finally becoming a single phase. The distinction between this newly created phase and the former one is still visible until the end of the convex part, where the particle surface becomes fully covered by the new phase. Although temperature is expected to increase as luminosity increases again, the change in surface emissivity due to the creation of a new phase prevents drawing any conclusion about an increase in temperature.

During the concave section, the rate of increase of the size evolution is constant while that of the luminosity increases progressively (see Fig. 4b), and the particle surface remains homogeneous while becoming brighter. Accordingly, no sudden surface emissivity change as observed during the convex section occurs due to the appearance of another phase at the surface, and the particle temperature increases at an increasing rate. The concave section ends when reaching the second peak, called 'large peak', which occurs when the peak luminosity is reached. Just before that large peak, a sudden luminosity jump takes place, which is



(a) Luminosity evolution and combustion snapshots of a 44 µm Fe-7Si particle.



(b) Size-normalized luminosity evolution of a 40 µm Fe-7Si particle.

Fig. 4. Multi-peak luminosity evolution observed during the single-particle combustion of (a) a 44 µm Fe-7Si particle including combustion snapshots and (b) a 40 µm Fe-7Si particle including size-normalized luminosity evolution. After laser heating, the particles reach a first small peak, followed by a decrease in luminosity, during which temperature decreases. The second rising part to the large peak is then constituted of two parts with a convex and concave shape, respectively. During the convex part, a new oxide phase is created and grows at the surface, while the surface is homogeneous during the concave part. The increase in temperature during this concave section becomes more significant when approaching the large peak, reached after a sudden luminosity jump associated with an instantaneous inflation, and followed by cooling until solidification.

attributed to a sudden particle size increase (see Fig. 4b), suggested to result from the creation of internal gas [23].

After the large peak, the particle cools down until it reaches solidification. Although solidification is usually identified by a luminosity jump [3] due to a sudden temperature increase after the solidification of a supercooled iron oxide droplet, it is here replaced by a luminosity drop (see Fig. 4a). The latter is due to a decrease in size during solidification caused by the sudden ejection of a gas (see Supplementary Information SI3), potentially the gas created just before the peak. This is justified by the fact that other Fe-7Si particles without sudden inflation before the peak show a luminosity jump at solidification, proving that the solidification of a supercooled iron oxide droplet still takes place. Nevertheless, while it is usually paired with a size increase due to the temperature jump [3], if the created gas is ejected, the impact on the particle size may be bigger than that of temperature. Therefore, whether solidification manifests as a luminosity jump or drop depends on the amount of gas released (leading to a size decrease) relative to the temperature increase.

Due to the decreasing luminosity level during cooling and the impossibility of collecting burned particles from this single-particle setup, no information about the reached oxidation level and combustion products' microstructure can be obtained. This limitation is mitigated by the results obtained with the multi-particle setup, as described in the next section.

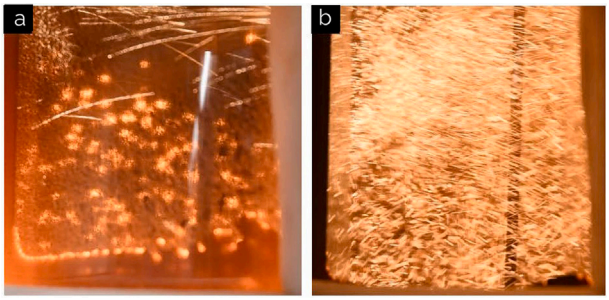


Fig. 5. Flame visualization inside the multi-particle burner during (a) test LT (810°C) and (b) test HT (930°C). Only few ignited particles are visible during test LT, while an established and stable flame was present during test HT.

3.2. Multi-particle combustion results

3.2.1. Flame analysis

Two combustion tests with the same Fe-7Si powder were conducted inside a multi-particle burner with two different preheating temperatures: 810°C (test LT) and 930°C (test HT). As illustrated in Fig. 5, a stable tornado-shaped flame was observed during test HT, while only localized ignition occurred during test LT (fewer red and bright particles). This highlights that ignition was barely achieved during test LT.

Subsequently, the gas temperature measured by the three thermo-couples (top, center, exhaust) and the O_2 concentration follow a different evolution between the two tests (see Fig. 6). During test LT, the gas temperature at the center of the chamber decreases below the defined temperature of 810°C after powder injection, while it increases above 930°C during test HT. The increase in temperature above the defined preheating temperature in that case implies that the powder at least partially ignited. The following evolution of the top and center temperatures is irregular, likely due to a heterogeneously distributed ignition inside the particle flow. This leads to a heterogeneous distribution of the temperature along the combustion chamber as observed by the exhaust temperature being lower by several hundred degrees. The difficult ignition during test LT is also consistent with the oxygen concentration measured by the gas analyzer at the exhaust: the concentration barely shifts from the initial concentration during test LT, while it decreases more significantly during test HT.

3.2.2. Collection of the combusted products

As illustrated in Fig. 7, the proportion of large agglomerates (>140 μm) in the combustion products is larger for the powders collected on the walls, especially for test HT at 22.57 wt.% compared to 1.94 wt.% for agglomerates collected from the walls and the cyclone collector. Also, the proportion of powder sticking to the burner walls is higher for test HT (85.5 g) than for test LT (38.3 g). These formed agglomerates were already observed in previous studies using the same burner [17,33]. Yet, the influence of Si on sintering and sticking tendency should be specifically analyzed in a dedicated study.

3.2.3. Microstructural analysis

XRD measurements. The phase distribution of one sample from each test and collection zone (four samples in total) reveals differences in oxidation levels between tests, and between the cyclone and combustion chamber (see XRD measurements in Fig. 8 and Table 3). Current XRD results can be analyzed using a conversion efficiency, which is defined based on the oxidation level reached by the particles, assuming that 100% oxidation is associated with Fe_2O_3 and SiO_2 (while 90% corresponds to Fe_3O_4 and Fe_2SiO_4 and 66% to FeO, based on the energy released).

Consistent with the temperature and oxygen concentration data (see Fig. 6), powders from test LT exhibit low oxidation, especially for the particles collected from the cyclone (0.2 wt.% oxidized to FeO). Particles collected from the chamber walls show higher oxidation (0.1 wt.% FeO + 2.3 wt.% Fe_3O_4 + 1.6 wt.% Fe_2SiO_4 + 2.6 wt.% Fe_2O_3). No SiO_2 phase is detected by XRD, likely due to its vitreous, non-crystalline state, and metallic Si remains alloyed with α-Fe. Traces (<3 wt.%) of a fayalite phase (Fe_2SiO_4) are, however, observed. For test HT, oxidation is higher in both collection locations, though a substantial fraction of α-Fe remains (70.5 wt.% from the cyclone and 57.8 wt.% from the walls). Again, powders collected from the walls show a higher oxidation level, with a marked increase in Fe_2O_3 content (+9.3 wt.%).

The resulting conversion efficiency can be compared with the results obtained with pure Fe particles (see Table 3). The conversion efficiency ranges between 0.1% and 6.2% for test LT and between 26.3% and 39%

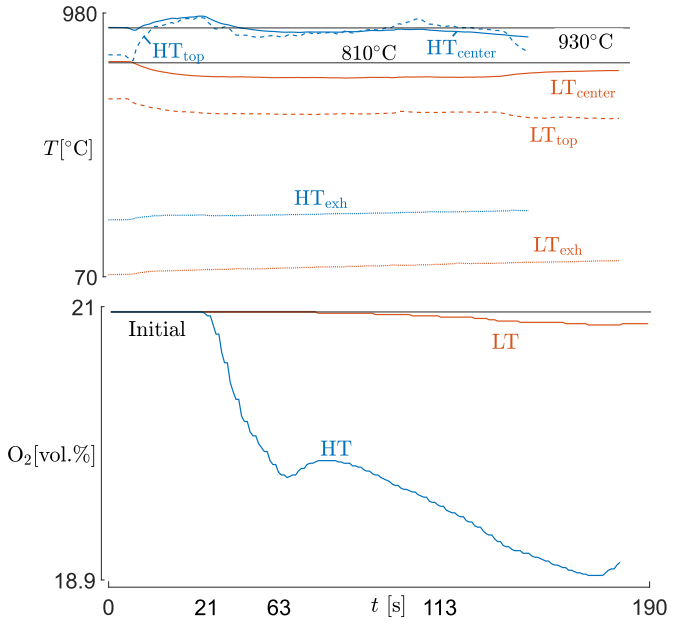


Fig. 6. Evolution of the temperature (upper graph) measured by the three thermo-couples inside the multi-particle burner and of the O_2 concentration (lower graph) measured by the gas analyzer during the two tests, represented by blue and Orange lines for HT and LT, respectively. (For interpretation of the references to colour in this Figure legend, the reader is referred to the web version of this article.)

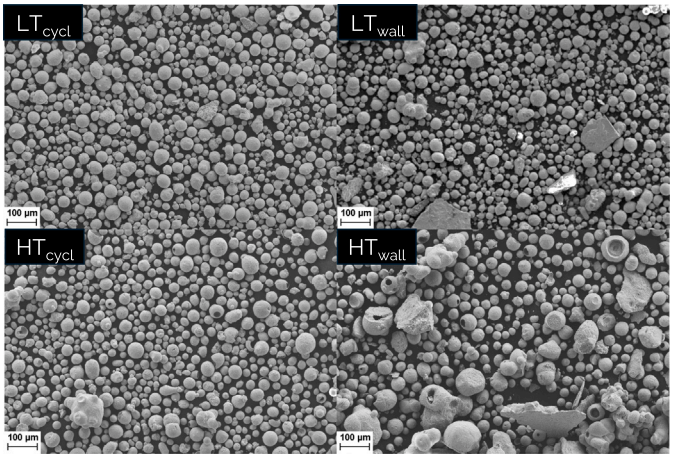


Fig. 7. Global SEM images of combustion products collected after the two tests inside the multi-particle burner from both the cyclone collector and the walls. Agglomerates are more prevalent for the powders collected on the walls, especially for test HT.

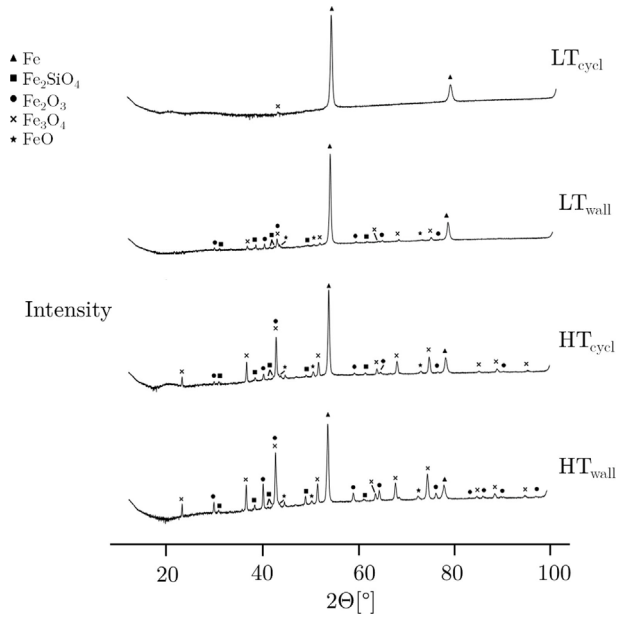


Fig. 8. XRD curves of combusted Fe-7Si powder in the tornado burner during the LT and HT tests collected from the walls and the cyclone.

Table 3
Phase composition and resulting conversion efficiency of the collected samples from the cyclone collector and from the walls for each test measured using XRD. The conversion efficiency of the powders collected on the walls is higher due to their higher residence time at high temperatures. Similar results obtained with pure Fe particles have been added for comparison.

Phase [wt.%]	LT_{cycl}	LT_{wall}	HT_{cycl}	HT_{wall}	[32]	[33]
Fe	99.8	93.5	70.5	57.8	4	9
FeO	0.2	0.1	2.1	0.8	–	4
Fe_3O_4	–	2.3	22.5	27.1	50	42
Fe_2SiO_4	–	1.6	1.9	2	–	–
Fe_2O_3	–	2.6	3	12.3	46	45
Conversion eff.	0.1%	6.2%	26.3%	39%	91%	85.4%

for test HT. This is much lower than the efficiency obtained in pure Fe experiments (>85%) using the same burner and similar experimental conditions [32,33].

The higher oxidation level observed on powders collected from the walls is primarily due to solid-state oxidation, as demonstrated by the larger hematite content in the powders collected from the walls, which can only form by solid-state oxidation. Particles adhering to the walls remain longer at elevated temperatures (>810°C for LT, >900°C for HT), allowing oxidation to proceed regardless of whether they were ignited. The extended residence time may also improve conversion efficiency, contributing to the higher overall oxidation.

SEM analysis. The XRD results suggest that most particles remain unignited, even in test HT. Nevertheless, the measured iron content in the XRD analysis comes not only from the non-ignited particles, but also partially from the unburnt iron core inside quenched particles (see Fig. 9). Yet, beyond those quenched particles still containing unburnt iron, the majority of oxidized particles are fully constituted by an oxide phase.

While non-ignited particles, recognizable by their random shapes, as they did not reach the liquid state, from test LT exhibit a homogeneous metallic surface (see Fig. 10a), those from test HT display darker spots on the metallic surface (see Fig. 10b). These spots correspond to an Si-enriched oxide phase relative to the initial composition.

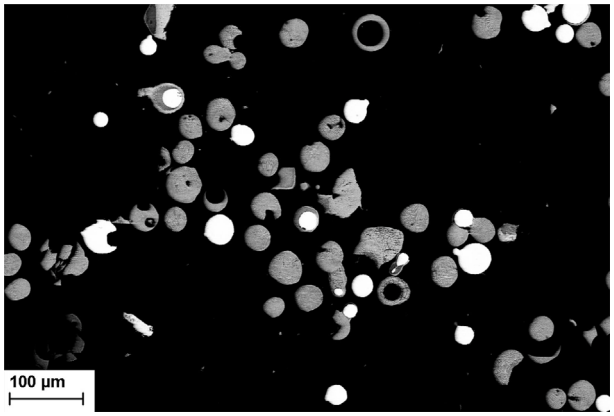


Fig. 9. Mapping of cross-section of the combustion products collected in the cyclone from test HT. It shows fully oxidized particles (grey), non-ignited particles (white), and quenched particles (white spherical iron core with a grey oxide layer). (For interpretation of the references to colour in this Figure legend, the reader is referred to the web version of this article.)

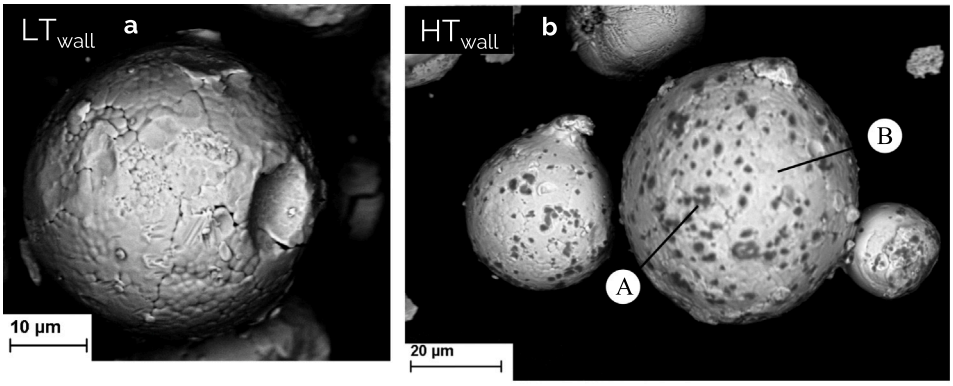
Ignited particles can be identified and analyzed, particularly in test HT. While non-ignited particles exhibit a smooth surface, sometimes with darker spots, ignited particles display dendritic structures on their surfaces (Fig. 11a and c). Dendritic microstructures are also observed in cross-sections (Fig. 11b and d). The volumetric distribution of dendrites and interdendritic phases depends on the composition of the liquid before solidification, while the particle cooling rate influences the number of dendrite nucleation points and their thickness, explaining observed variations in dendrite morphology. Additionally, a eutectic phase is visible within the interdendritic regions (see magnified images in Fig. 11b and d), indicating that the liquid reached a eutectic point during cooling and solidification.

The composition of the eutectic phase has been measured using EDS (see Fig. 12). The spatial resolution of EDS (~1 μm^3) is not sufficient to resolve the very fine eutectic microstructure; however it gives the average composition of the liquid undergoing the eutectic transformation. To improve the reliability of these measurements, they were repeatedly conducted on four particles, with the three other particles showing values consistent with the one presented in Fig. 12 (see Supplementary Materials SM4). For both the dendrites and the eutectic phase, the measured EDS signal shows an oxide with both Fe and Si, with Si enrichment in the eutectic microstructure (between 7.5 wt.% and 9.7 wt.% Si, not accounting for point 7 in Fig. 12 as it shows slightly higher Si concentration compared to all other points). This enrichment is visible in SEM images of Fig. 11 as Si oxide appears darker than Fe oxide. As EDS is not a good tool to measure light elements quantitatively, it is mainly used here to compare Fe with Si and to find possible enriched zones while providing qualitative measurements of oxygen. This explains the lower oxygen content measured by EDS relative to the expected value corresponding to the Fe_3O_4 phase (~28 wt.%) measured by XRD. Therefore, the phase obtained for the dendrites is likely magnetite.

4. Discussion

4.1. Influence of preheating temperature on conversion efficiency

Combustion tests in the multi-particle burner show that 7 wt.% Si significantly hinders the conversion efficiency. Using the same conditions as for pure iron (preheating temperature of 810°C), the conversion efficiency is limited to 0.1%–6.2%, compared to more than 85% for pure Fe particles. This suggests that the presence of Si prevents a proper powder ignition, as also evidenced by the unstable character of the formed flame. Increasing the preheating temperature by 120°C enabled an increase in the conversion efficiency (to 26.3%–39%), suggesting that ignition of a larger fraction of particles was reached, forming a stable flame.



wt.%	Fe	Si	O
A	55.8	20	24.2
B	95.1	4.1	0.8

Fig. 10. Non-ignited particles collected from the walls during tests (a) LT and (b) HT. For the particle from test HT, the surface chemical composition shows Si-rich darker oxide spots on top of a metallic surface.

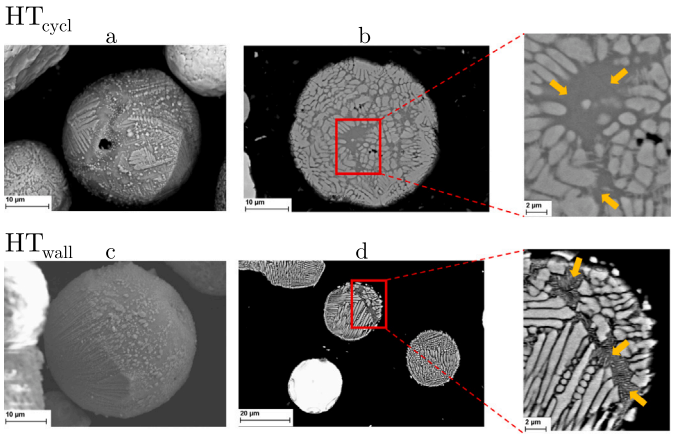


Fig. 11. SEM images of the ignited particles collected after the HT test, both from the (a-b) cyclone collector and (c-d) the walls. The surface of ignited particles shows dendrites, which can also be found in their internal microstructure. In addition, a eutectic phase is present inside the interdendritic phase (yellow arrows). (For interpretation of the references to colour in this Figure legend, the reader is referred to the web version of this article.)

As non-ignited particles show Si-rich surface spots (see Fig. 10b), Si oxidation plays a key role in the ignition behavior. Previous observations of Fe–Si oxidation between 900–1050°C [35] also showed that the presence of Si induces the formation of an intermediate mixed Fe–Si oxide layer, and that a thin silica layer in contact with the metal is typically formed.

The migration of Si from the core to the surface during solid-state oxidation likely results from the preferential oxidation of silicon, which has a higher oxygen affinity than iron [36]. Then, the limited diffusion of silicon within silica allows iron cations to diffuse faster, forming a mixed oxide layer [35]. However, iron diffusion through silica (10^{-13} cm^2/s) is much slower than through iron oxides (10^{-8} cm^2/s) [37,38], strongly reducing oxidation kinetics compared to pure iron combustion. This mitigated oxidation rate likely contributes to poor powder ignition.

Given that an increase in preheating temperature improved the conversion efficiency, higher temperatures are expected to improve it even more. By increasing the temperature, iron diffusion through the silica layer would be accelerated, promoting ignition. This is also expected due to the successful ignition observed when using laser heating in the single-particle setup, which heats the particles to a much higher temperature (above the melting point). Moreover, dedicated ignition analysis should be conducted to better understand the effect of Si on the solid-state oxidation kinetics, for example using thermogravimetric analysis at different preheating temperatures.

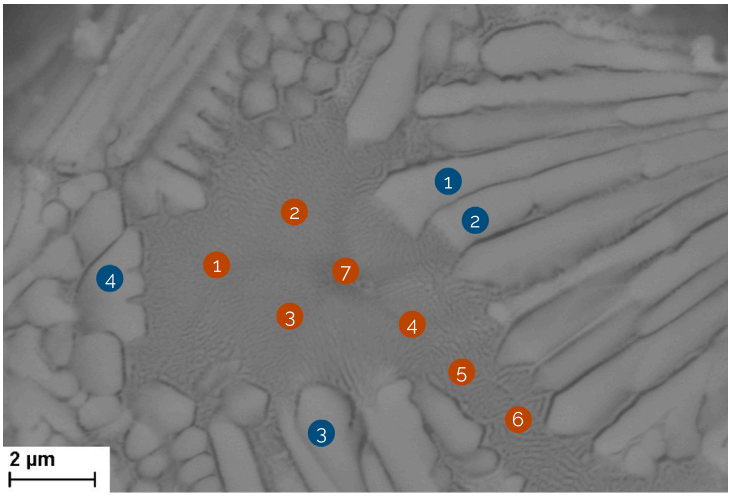
4.2. Combustion regime

In the single-particle setup, laser heating overcomes the difficulties of powder ignition, enabling the study of liquid-state combustion. As observed by Peng et al. [22], a first luminosity peak occurs shortly after ignition, followed by a rapid decrease in luminosity and temperature. Their hypothesis that this drop results from the formation of a Si-rich oxide layer reducing the oxidation rate is consistent with the higher oxygen affinity of silicon compared to iron [36] and the low diffusion coefficients of Fe and Si within a Si-rich oxide layer [39].

Assuming a diffusion coefficient of approximately 10^{-5} cm^2/s for iron in liquid silica (consistent with experimentally determined Fe diffusion coefficients in molten oxide/silicate systems at high temperatures [40,41]) and considering the 0.7–1.1 ms duration of the luminosity decrease, the corresponding diffusion thickness is around 1.2 µm to 1.5 µm. Regarding the thickness of a few µm measured on quenched particles collected in the cyclone after test HT (see Fig. 13), the formation of a Si-rich oxide layer of this thickness is plausible and could explain the observed drop. For those particles, the spherical shape of the inner iron core suggests that ignition and melting occurred, but the particles likely quenched before fully oxidizing in the liquid state. Nevertheless, the oxidation state of this created Si-rich oxide phase remains uncertain, while single-particle results for pure Si combustion suggest that the formation of SiO is favored over SiO_2 [42].

During the luminosity drop following the initial small peak, the particle surface darkens and its size decreases, indicating a temperature decrease likely caused by a reduced oxidation rate due to the formation of a Si-rich oxide layer. Peng et al. [22] proposed that the particle burns in an internal-diffusion-limited regime, but no additional evidence from this study allows for confirmation of that mechanism.

The subsequent luminosity increase after a few milliseconds indicates that iron oxidation continues. This rise coincides with the appearance of a new, bright oxide phase on the particle surface. The brief luminosity drop can thus be explained by slower oxidation and limited diffusion to



[wt.%]	Fe	Si	O
1	79.48	2.35	18.17
2	80.43	2.28	17.29
3	79.31	2.88	17.81
4	78.99	2.88	18.13
1	71.95	8.65	19.39
2	72.08	8.4	19.52
3	71.33	8.9	19.77
4	71.5	8.91	19.59
5	72.13	8.37	19.5
6	71.29	9.18	19.53
7	68.73	11.54	19.72

Fig. 12. EDS analysis of the composition of the dendrites and the eutectic phase observed in combusted Fe-7Si particles. It shows that for both the dendrites and the eutectic phase, the measured EDS signal indicates an oxide containing both Fe and Si, with Si enrichment in the eutectic microstructure.

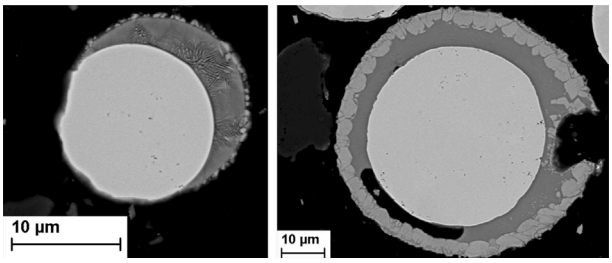


Fig. 13. SEM images of the cross-section of quenched Fe-7Si particles collected from the cyclone after test HT. The spherical shape of the inner iron core proves that ignition and melting occurred, but they did not fully oxidize, likely due to quenching. Regarding the thickness of 3 µm to 5 µm of the oxide layer, this is in the same order of magnitude as the estimated minimum thickness of Si-rich oxide layer created at the beginning of the combustion.

the surface, while the following increase may result from the growing coverage of the bright phase and possibly from a temperature rise, although the latter cannot be confirmed. The initial convex portion of this rise is therefore attributed primarily to changes in surface emissivity, as the new phase appears more rapidly at the surface at the beginning.

Once the particle surface is fully covered, the convex portion of the luminosity evolution transitions into a concave shape. The slope of the luminosity increases with time while particle size continues to grow steadily, suggesting a rise in particle temperature that likely began during the convex section. However, the lower slope compared to the initial post-ignition rise indicates that the rate-limiting mechanism now involves not only external oxygen diffusion to the surface but also internal diffusion of metallic species.

A notable difference from Peng et al. [22] is the absence of intermediate jumps between small peaks in our luminosity data, previously attributed to intermediate solidification and re-melting. This discrepancy is likely due to particle size: particles in the current study range from 25 µm to 63 µm, whereas those in the previous study had a mean diameter of 119 µm. Larger particles experience greater heat loss during the luminosity drop, allowing their temperature to fall below the solidification point, whereas smaller particles maintain temperatures above solidification until the final reactive cooling phase.

4.3. Phases created

The combustion products of ignited particles consist mostly of magnetite, with hematite also present for the most oxidized ones. This indicates that once the ignition barrier is overcome, Fe–7Si particles can fully oxidize in the liquid state. Although no microstructural analysis was conducted in previous experiments with pure Fe particles using the same burner [32,33], the eutectic phase observed within the interdendritic matrix (see Fig. 11), whose interdendritic character has already been linked to the presence of SiO_2 [18], is a novel trait that was not observed for pure Fe particles [43]. We suggest that it results from the rapid solidification of an Fe-Si-O liquid phase, as detailed below.

All the phases expected in the system Fe-Si-O were detected by XRD (see Table 3), *i.e.,* metallic α-Fe, wüstite $Fe_{(1-x)}O$, magnetite Fe_3O_4, hematite Fe_2O_3 and fayalite Fe_2SiO_4. The only missing phase is tridymite/cristobalite SiO_2. Yet, the presence of glassy SiO_2 (instead of crystalline tridymite/cristobalite) was previously reported after quenching of Fe-Si-O oxide liquid phase at the end of a combustion process [18]. Therefore, it would not be surprising if XRD did not detect the presence of SiO_2. According to the thermodynamic simulation of adiabatic combustion of Fe-7Si [14], the microstructure expected at the end of the combustion of a fully oxidized liquid Fe-Si-O phase is (i) the formation of Fe_3O_4 dendrites (from 1776 K), followed by (ii) a eutectic transformation of the remaining oxide liquid phase, enriched in Si, into a mixture of Fe_3O_4 and SiO_2 (at 1713 K). Further solid-state oxidation will gradually transform Fe_3O_4 into Fe_2O_3. This prediction fits well with the observed microstructure of the ignited particles, composed of a majority of Fe-rich oxide dendrites (see Fig. 12), and with the XRD measurements (see Table 3), which detect Fe_3O_4 as the main stabilized oxide. In the interdendritic region, a eutectic microstructure is observed, composed of a fine mixture between a dark Si-rich oxide phase and a phase of similar contrast to the dendrites, *i.e.,* probably magnetite.

The Fe-Si-O system contains 5 invariant points associated with a fast solidification process that could produce a fine microstructure such as the one observed in the interdendritic region [44]. The solidification path chosen by the liquid oxide phase will depend on its composition at the onset of solidification, while the composition of the final fine microstructure is fixed for each invariant point. For increasing Si concentration of the invariant point, the phases formed are: (a) Liquid + Fe_3O_4 + SiO_2 (reported between 7.4 wt.% Si and 9 wt.% Si); (b) Liquid + Fe_2SiO_4 + $Fe_{(1-x)}O$ + Fe (10.5 wt.% Si); (c) Liquid + Fe_2SiO_4 + $Fe_{(1-x)}O$ + Fe_3O_4 (12.2 wt.% Si); (d) Liquid + Fe_2SiO_4 + SiO_2 + Fe_3O_4 (15.3 wt.% Si); (e) Liquid + Fe_2SiO_4 + Fe + SiO_2 (17.3 wt.% Si). Local EDS measurements of the fine interdendritic microstructure estimated local concentrations varying between 7.5 wt.% Si and 9.7 wt.% Si. These measurements should be used with caution as the interdendritic region approaches the limits of the spatial resolution of EDS (~1 μm^3) and because EDS does not quantify light elements such as oxygen.

A characterization of the local phase at the nanometric scale is required to formally identify the phases within the interdendritic region, which is outside the scope of the present study. Nevertheless, the qualitatively low concentration of Si in the interdendritic region indicates that it probably corresponds to the invariant point (a), *i.e.,* the eutectic transformation thermodynamically predicted when the Fe-7Si particles are fully oxidized in the liquid phase. The presence of $Fe_{(1-x)}O$ and Fe_2SiO_4 indicates that some particles could also follow the invariant point (b), corresponding to particles quenched before their full oxidation in the liquid state. It should be noted that both $Fe_{(1-x)}O$ and Fe_2SiO_4 could also form during the solid-state oxidation of non-ignited particles.

Although the addition of Si increases the theoretical heat release of Fe–Si particles (32.4 MJ/kg for Si → SiO_2, compared with 6.7 MJ/kg for Fe → Fe_3O_4 and 7.4 MJ/kg for Fe → Fe_2O3), the actual energy output is strongly constrained by the low conversion efficiency. At the highest conversion efficiency obtained in this study (39% for HTwall), the heat release reaches only 3.4 MJ/kg, which remains well below the 6.9 MJ/kg obtained with pure iron under similar multi-particle burner conditions [33]. Assuming oxidation of Fe and Si to Fe_3O_4 and SiO_2, respectively, a conversion efficiency of at least 81.2% would therefore be required for Fe-7Si particles to match the specific heat release of pure Fe particles. At 100% conversion efficiency, the theoretical heat release would reach 8.5 MJ/kg. These results highlight the importance of achieving high conversion efficiency to fully exploit the energy potential of Si-containing iron powders, which requires ensuring sufficient ignition. However, achieving a higher ignition efficiency may require higher air preheating temperatures, which introduce an additional energy penalty. To assess whether this penalty is offset by the additional heat released through Si oxidation, the two effects can be compared by considering complete oxidation of Fe and Si to Fe_3O_4 and SiO_2, respectively, and a stoichiometric amount of air heated from ambient temperature to the required preheating temperature. Under these assumptions, the additional heat release provided by the 7 wt.% Si in Fe-7Si compensates for the additional energy required to preheat the air up to approximately 1663°C. Thus, from an energy-output perspective, Fe-7Si particles remain potentially advantageous over pure Fe provided that sufficiently high conversion efficiency can be achieved. Nevertheless, the higher preheating temperature may introduce an economic trade-off between the potential savings associated with lower-cost iron-based feedstocks and the additional energy required for preheating. A detailed techno-economic assessment of this trade-off is beyond the scope of the present study and is left for future work.

4.4. Expected influence on reduction

Concerning the reduction of oxidized Fe-7Si particles, Si oxide impurities are expected to adversely affect the reduction kinetics of combusted Fe oxides, primarily due to the low reducibility of the complex ternary oxide phases that form [45,46]. Even if SiO_2 doping in hematite pellets initially increases porosity [47,48], which enhances the reduction rate, it is decreased at reduction temperatures above 1300°C due to local melting [49,50]. During reduction, SiO_2 reacts with Fe oxides to form silicates (*e.g.*, Fe_2SiO_4), which are less reducible and decrease porosity [45,47,48,50]. Si-rich phases can also form dense surface or interfacial layers that significantly hinder reduction [51].

Furthermore, Si can be considered within an open-system framework. For instance, when recycled Si-containing steel scrap is used as a fuel source, the resulting oxidized powder can be reduced in blast furnaces, where SiO_2-rich slags are routinely processed.

5. Conclusion

This study advances the understanding of the combustion behavior of micron-sized Fe–7Si particles. First, *in situ* high-speed imaging and luminosity measurements during single-particle combustion showed that liquid-state oxidation rapidly becomes limited, which is suggested to result from the creation of a Si-rich oxide layer mitigating the internal diffusion of Si and Fe toward the surface. After a short moment during which the temperature likely decreases while oxidation continues, a new Fe-rich oxide phase arises at the particle surface and progressively covers the former phase. Combustion thereafter continues and the temperature increases until it reaches a large peak, followed by reactive cooling and solidification.

The tests conducted inside the multi-particle burner highlighted that the presence of 7 wt.% Si limits the conversion efficiency (0.1%–6.2%) when preheating the gases to the same temperature as for pure Fe (810°C). *Ex situ* analysis of non-ignited particles revealed that Si-rich oxide spots were created at the particle surface, potentially mitigating the internal diffusion and so the oxidation rate. Nevertheless, an improved conversion efficiency (26.3%–39%) was reached by increasing the preheating temperature to 930°C. Examination of the solidified products revealed that they are mostly composed of magnetite, with the potential presence of fayalite. Microstructure analysis showed that the combusted particles are made of a dendritic microstructure surrounding a Si-enriched eutectic phase inside the interdendritic matrix. The measured composition of this phase suggests that full oxidation in the liquid state is reached prior to reaching the eutectic point during cooling and solidification.

These findings indicate that silicon alters the rate-controlling mechanism of combustion, shifting it toward enhanced internal diffusion and thereby extending the overall combustion time compared with pure iron. Yet, they also prove that ignited particles reach a high oxidation degree. Future studies should be dedicated to understanding the solid-state oxidation kinetics close to the ignition temperature of such particles and to the design of efficient ignition system.

CRediT authorship contribution statement

Z. Bruyr: Writing – original draft, Visualization, Software, Resources, Methodology, Investigation, Funding acquisition, Conceptualization. **L. Ahmad:** Writing – review & editing, Visualization, Resources, Methodology, Investigation. **L. Choisez:** Writing – review & editing, Supervision, Resources, Investigation, Conceptualization. **M. Gilles:** Visualization, Methodology, Investigation. **L. Jeanmart:** Visualization, Methodology, Investigation. **F. Halter:** Writing – review & editing, Supervision, Resources, Conceptualization. **F. Contino:** Writing – review & editing, Supervision, Resources, Funding acquisition, Conceptualization.

Declaration of competing interest

The authors declare the following financial interests/personal relationships that may be considered potential competing interests:

Zakarie Bruyr reports that financial support was provided by the Fund for Scientific Research. Laurine Choisez reports that financial support was provided by the Fund for Scientific Research. If there are other authors, they declare that they have no known competing financial interests or personal relationships that could have appeared to influence the work reported in this paper.

Acknowledgements

The authors acknowledge Hugo Keck and Willie Prasidah for their help in the manipulation of the single-particle and multi-particle experimental setups, respectively. This work has received funding from the Fonds de la Recherche Scientifique - FNRS. ZB acknowledges financial support through an F.R.S.-FNRS doctoral mandate. LC acknowledges financial support through an F.R.S.-FNRS chargée de recherche mandate (ID40011141).

Appendix A. Supplementary data

Supplementary data to this article can be found online at doi:10.1016/j.fuel.2026.141936.

XPS measurements of the surface chemical composition, detailed methodology for particle size measurement using the single-particle setup, analysis of the luminosity drop at solidification, and additional EDS composition measurements of the dendrites and the eutectic phase.

Data availability

Data will be made available on request.

References

[1] Clarke L, Wei Y-M, Navarro ADLV, Garg A, Hahmann A, Khennas S, Azevedo I, Löschel A, Singh A, Steg L, Strbac G, Wada K. Energy systems. In: Shukla P, Skea J, Slade R, Khourdajie AA, van Diemen R, McCollum D, Pathak M, Some S, Vyas P, Fradera R, Belkacemi M, Hasija A, Lisboa G, Luz S, Malley J, editors. Climate change 2022: mitigation of climate Change. Contribution of working group III to the sixth assessment report of the intergovernmental panel on climate change. Cambridge, UK and New York, NY, USA: Cambridge University Press; 2022.

[2] Bergthorson J, Goroshin S, Soo M, Julien P, Palecka J, Frost D, Jarvis D. Direct combustion of recyclable metal fuels for zero-carbon heat and power. Appl Energy 2015. [Online]. Available: 160:368–82. https://www.sciencedirect.com/science/article/pii/S0306261915011071.

[3] Ning D, Shoshin Y, van Oijen J, Finotello G, de Goey P. Size evolution during laser-ignited single iron particle combustion. Proc Combust Inst 2023;39(3):3561–71. [Online]. Available: https://www.sciencedirect.com/science/article/pii/S1540748922000724.

[4] Ning D, Shoshin Y, van Oijen J, Finotello G, de Goey L. Burn time and combustion regime of laser-ignited single iron particle. Combust Flame 2021. [Online]. Available: 230:111424. https://www.sciencedirect.com/science/article/pii/S0010218021001607.

[5] Ning D, Shoshin Y, van Stiphout M, van Oijen J, Finotello G, de Goey P. Temperature and phase transitions of laser-ignited single iron particle. Combust Flame 2022. [Online]. Available: 236:111801. https://www.sciencedirect.com/science/article/pii/S0010218021005447.

[6] Panahi A, Chang D, Schiemann M, Fujinawa A, Mi X, Bergthorson JM, Levendis YA. Combustion behavior of single iron Particles–Part I: An experimental study in a drop-tube furnace under high heating rates and high temperatures. Appl Energy Combust Sci 2022. [Online]. Available: 100097. https://www.sciencedirect.com/science/article/pii/S2666352X22000401.

[7] Hameete J, Abdallah M, Thijs L, Homan T, Mi X, Dam N, de Goey L. Particle-resolved hyperspectral pyrometry of metal particles. Combust Flame 2024. [Online]. Available: 264:113435. https://www.sciencedirect.com/science/article/pii/S0010218024001445.

[8] Bruyr Z, Hameete J, Choisez L, Halter F, Contino F. Observation of an unmixed particle surface during single-particle experiments of iron combustion. Fuel 2025. [Online]. Available: 395:135261. https://www.sciencedirect.com/science/article/pii/S001623612500986X.

[9] Thijs L, van Gool C, Ramaekers W, van Oijen J, de Goey L. Resolved simulations of single iron particle combustion and the release of nano-particles. Proc Combust Inst 2023;39(3):3551–9. [Online]. Available: https://www.sciencedirect.com/science/article/pii/S1540748922000682.

[10] Thijs LC, van Gool CEAG, Ramaekers WJS, Kuerten JGM, van Oijen JA, de Goey LPH. Improvement of heat- and mass transfer modeling for single iron particles combustion using resolved simulations. Combust Sci Technol 2024. [Online]. Available: 196(4):572–88. https://doi.org/10.1080/00102202.2022.2089030

[11] Fujinawa A, Thijs LC, Jean-Philyppe J, Panahi A, Chang D, Schiemann M, Levendis YA, Bergthorson JM, Mi X. Combustion behavior of single iron particles, Part II: A theoretical analysis based on a zero-dimensional model. Appl Energy Combust Sci 2023. [Online]. Available: 14:100145. https://www.sciencedirect.com/science/article/pii/S2666352X23000341.

[12] Thijs LC, Kritikos EM, Giusti A, Ramaekers G, van Oijen JA, de Goey P, Mi X. On the surface chemisorption of oxidizing fine iron particles: insights gained from molecular dynamics simulations. Combust Flame 2023. [Online]. Available: 254:112871. https://www.sciencedirect.com/science/article/pii/S0010218023002523.

[13] Thijs LC, Van Ende M-A, van Oijen JA, de Goey P, Mi X. A numerical study of internal transport in oxidizing liquid core–shell iron particles. Combust Flame 2025. [Online]. Available: 271:113826. https://www.sciencedirect.com/science/article/pii/S0010218024005352.

[14] Choisez L, Van Ende M-A, Bruyr Z, Contino F, Jacques PJ. Influence of impurities on the use of FE-based powder as sustainable fuel. Philos Trans R Soc A Math Phys Eng Sci 2024. [Online]. Available: 382(2284):20230236. https://royalsocietypublishing.org/doi/abs/10.1098/rsta.2023.0236.

[15] Bruyr Z, Choisez L, Thijs L, Mi X, Jacques P, Halter F, Contino F. Combustion of a single iron-based impure particle: numerical analysis of four non-volatile oxide impurities using a parametric approach. Fuel 2026. [Online]. Available: 407:137277. https://www.sciencedirect.com/science/article/pii/S0016236125030029.

[16] Choisez L, Kuypers B, Stevens N, Prasidha W, Mauxion T, de Goey P, Finotello G, Jacques PJ. On the use of industrial steel mill scale as a high-density energy carrier: Part II. microstructural and chemical evolution over cycling. Fuel 2026. [Online]. Available: 406:136906. https://www.sciencedirect.com/science/article/pii/S0016236125026316.

[17] Choisez L, Stevens N, Prasidha W, Kuypers B, Mauxion T, de Goey P, Finotello G, Jacques PJ. On the use of industrial steel mill scale as a high-density energy carrier: Part I. reaction processes and particle size evolution over cycling. Fuel 2026. [Online]. Available: 405:136614. https://www.sciencedirect.com/science/article/pii/S0016236125023397.

[18] Ahmad L, Bruyr Z, Contino F, Jacques PJ, Choisez L. On the pore formation during the combustion of direct reduced iron powders. Steel Res Int 2026;97(8):4337–50. [Online]. Available: https://onlinelibrary.wiley.com/doi/abs/10.1002/srin.202501334.

[19] Bruyr Z, Ahmad L, Choisez L, Halter F, Contino F. Influence of al as an alloying element on the combustion process of micron-sized iron particles. Fuel 2026. [Online]. Available: 422:139083. https://www.sciencedirect.com/science/article/pii/S0016236126008367.

[20] Karami R, Butler D, Tamimi S. Manufacturing of non-grain-oriented electrical steels. Int J Adv Manuf Technol 2024;133(3):1083–109.

[21] Müller M, Bailly D, Hirt G. Microstructure evolution and magnetic properties of a 4.5 wt% silicon steel produced by twin-roll casting. Steel Res Int 2022. [Online]. Available: 93(11):2200554. https://onlinelibrary.wiley.com/doi/abs/10.1002/srin.202200554.

[22] Peng F, Kong C, Liu H, Mi X, Xu S, Liu Y, Cai W. Ignition and combustion of a single iron particle with impurities in hot post-flame gas flow. Combust Flame 2024. [Online]. Available: 265:113509. https://www.sciencedirect.com/science/article/pii/S0010218024002177.

[23] Bruyr Z, Choisez L, Ahmad L, Eloy P, Halter F, Contino F. Influence of chemical additions and specific surface area on micro-explosion of burning iron particles. Energy Fuels 2026. [Online]. Available: 40(6):3382–96. https://doi.org/10.1021/acs.energyfuels.5c05699

[24] Keck H, Chauveau C, Legros G, Gallier S, Halter F. New experimental method for the simultaneous determination of concentration and size profiles of condensed combustion products around a burning aluminum droplet. Combust Flame 2024. [Online]. Available: 268:113616. https://www.sciencedirect.com/science/article/pii/S0010218024003250.

[25] Braconnier A. Étude expérimentale de la combustion d'une particule d'aluminium isolée: influence de la pression et de la composition de l'atmosphère oxydante [Ph.D. dissertation]. Mechanical Engineering; Oct 2020.

[26] Muller M, El-Rabii H, Fabbro R. Liquid phase combustion of iron in an oxygen atmosphere. J Mater Sci Jan 2015;50.

[27] Rhim W-K, Ohsaka K. Thermophysical properties measurement of molten silicon by high-temperature electrostatic levitator: density, volume expansion, specific heat capacity, emissivity, surface tension and viscosity. J Cryst Growth 2000. [Online]. Available: 208(1):313–21. https://www.sciencedirect.com/science/article/pii/S0022024899004376.

[28] Takasuka E, Tokizaki E, Terashima K, Kimura S. Emissivity of liquid silicon in visible and infrared regions. J Appl Phys 1997;81(9):6384–9.

[29] Petrov V, Vorobyev A. Spectral emissivity and radiance temperature plateau of self-supporting al_2O_3 melt at rapid solidification. High Temp - High Press, vol. v. 35/36, pp. Jan 2007;321–9.

[30] Rozenbaum O, Meneses D, Auger Y, Chermanne S, Echegut P. A spectroscopic method to measure the spectral emissivity of semi-transparent materials up to high temperature. Rev Sci Instrum Oct 1999;70:4020–5.

[31] Prasidha W, Baigmohammadi M, Shoshin Y, de Goey P. Optimizing iron powder combustion: influence of particle size on flame stability, nanoparticle formation, and nitric oxide emission. Combust Flame 2025. [Online]. Available: 275:114068. https://www.sciencedirect.com/science/article/pii/S0010218025001063.

[32] Prasidha W, Baigmohammadi M, Shoshin Y, de Goey P. Towards an efficient metal energy carrier for zero–emission heating and power: iron powder combustion. Combust Flame 2024. [Online]. Available: 268:113655. https://www.sciencedirect.com/science/article/pii/S001021802400364X.

[33] Baigmohammadi M, Prasidha W, Stevens NC, Shoshyn YL, Spee T, de Goey P. Towards utilization of iron powders for heating and power. Appl Energy Combust Sci 2023. [Online]. Available: 13:100116. https://www.sciencedirect.com/science/article/pii/S2666352X23000055.

[34] Mi X, Fujinawa A, Bergthorson JM. A quantitative analysis of the ignition characteristics of fine iron particles. Combust Flame 2022. [Online]. Available: 240:112011. https://www.sciencedirect.com/science/article/pii/S001021802200030X.

[35] Abba A, Galerie A, Caillet M. Protection du fer contre l'oxydation par siliciuration superficielle. Mater Chem 1980. [Online]. Available: 5(2):147–64. https://www.sciencedirect.com/science/article/pii/0390603580900139.

[36] Ellingham HJT. Reducibility of oxides and sulfides in metallurgical processes. J Soc Chem Ind 1944;63(6):125–60.

[37] Wang P, Feng Y, Roth W, Corbett J. Diffusion behavior of implanted iron in fused silica glass. J Non-Cryst Solids 1988. [Online]. Available: 104(1):81–4. https://www.sciencedirect.com/science/article/pii/0022309388901858.

[38] Wang PW, Feng YP, Roth WL, Corbett JW. Diffusion behavior of implanted iron in fused silica glass. J Non-Cryst Solids 1988. [Online]. Available: 104(1):81–4. https://www.sciencedirect.com/science/article/pii/0022309388901858.

[39] Karki BB, Bhattarai D, Stixrude L. First-principles simulations of liquid silica: structural and dynamical behavior at high pressure. Phys Rev B Sep 2007. [Online]. Available: 76:104205. https://link.aps.org/doi/10.1103/PhysRevB.76.104205.

[40] Dunn T, Ratliffe WA. Chemical diffusion of ferrous iron in a peraluminous sodium aluminosilicate melt: 0.1 MPa to 2.0 GPa. J Geophys Res Solid Earth 1990;95(B10):15665–73.

[41] Ni H, Hui H, Steinle-Neumann G. Transport properties of silicate melts. Rev Geophys 2015;53(3):715–44.

[42] Heng H, Keck H, Chauveau C, Goroshin S, Bergthorson J, Halter F. Combustion behaviour of single silicon particles in different oxidizing environments. Combust Flame 2026. [Online]. Available: 283:114625. https://www.sciencedirect.com/science/article/pii/S0010218025006625.

[43] Choisez L, van Rooij NE, Hessels CJ, da Silva AK, Filho IRS, Ma Y, de Goey P, Springer H, Raabe D. Phase transformations and microstructure evolution during combustion of iron powder. Acta Mater 2022. [Online]. Available: 239:118261. https://www.sciencedirect.com/science/article/pii/S1359645422006413.

[44] Hidayat T, Shishin D, Decterov SA, Jak E. Experimental study and thermodynamic re-optimization of the FeO-fe_2O_3-sio_2 system. J Ph Equilibria Diffus 2017;38(4):477–92.

[45] Kim W-H, Lee Y-S, Suh I-K, Min D-J. Influence of CaO and sio_2 on the reducibility of wüstite using H2 and CO gas. ISIJ int 2012;52(8):1463–71.

[46] Bahgat M, Halim KSA, Nasr MI, El-Geassy AA. Morphological changes accompanying gaseous reduction of sio_2 doped wüstite compacts. Ironmak Steelmak 2008. [Online]. Available: 35(3):205–12. https://doi.org/10.1179/174328107X155259

[47] El-Geassy A-HA, Nasr MI, Omar AA, Mousa E-SA. Influence of sio_2 and/or MnO_2 on the reduction behaviour and structure changes of fe_2O_3 compacts with CO gas. ISIJ int 2008;48(10):1359–67.

[48] Halim KSA, Bahgat M, El-Kelesh HA, Nasr MI. Metallic iron whisker formation and growth during iron oxide reduction: basicity effect. Ironmak Steelmak 2009. [Online]. Available: 36(8):631–40. https://doi.org/10.1179/174328109X463020

[49] Ono-Nakazato H, Okada K, Usui T. Effects of slag content and composition on the reducibility of iron oxide including CaO-sio_2-FetO slag. ISIJ int 2005;45(4):569–73.

[50] Guo H, Jiang X, Shen F, Zheng H, Gao Q, Zhang X. Influence of sio_2 on the compressive strength and reduction-melting of pellets. Metals 2019. [Online]. Available: 9(8). https://www.mdpi.com/2075-4701/9/8/852.

[51] Shigematsu N, Iwai H. Effect of the addition of sio_2 and sio_2-CaO on the reduction of dense wustite at high temperatures. Tetsu-to-Hagané 1993;79(8):920–6.